

Research Article

Xu Shan*, Bin Miao, Zhe Cao, Zhenyu Sun, Yiren Li, Kai Liu, Sanbiao Qu, Xingyu Guo, Zhenpeng Su, Chenglong Shen, Zonghao Pan, Xin Li, Xinjun Hao, Xiaoping Yang, Chao Tian, Yu Jiang, Shubin Liu, Qi An, Xiangjun Chen, and Yuming Wang

A low-energy ion spectrometer with large field of view and wide energy range onboard a Chinese GEO satellite

<https://doi.org/10.1515/astro-2022-0210>

received July 24, 2022; accepted October 27, 2022

Abstract: A low-energy ion spectrometer (LEIS), onboard a Chinese navigation satellite in geosynchronous orbit, is one of the primary instruments for plasma detection. The LEIS is implemented by combining a top-hat electrostatic analyzer with a pair of angular scanning deflectors, which enables us to achieve *in situ* measurement of energetic ions in three-dimensional (3D) space with a large field of view of $360^\circ \times 90^\circ$ and a wide energy range from 50 eV to 25 keV per charge. The key performance parameters including analyzer constant, geometric factor, linear relation function between elevation angles and deflector voltages, and the energy or angular resolutions have been determined by using detailed simulations and calibration experiments on the ground. The preliminary results from on-orbit observations demonstrate that the capability of the present LEIS payload can well meet the mission requirements for sampling the low-energy ion distributions in 3D space, measuring the negative satellite surface potential, and monitoring the magnetospheric storm or substorm activities.

Keywords: low-energy ion spectrometer, Chinese geosynchronous satellite, space environment monitoring

1 Introduction

Space environment monitoring and weather forecast become extremely important for satellite safety. Charged particles in space are known to damage spacecraft and are regarded as a significant fraction of spacecraft anomalies (Baker 2000, Iucci *et al.* 2005, Quan *et al.* 2022). Galactic cosmic rays and solar energetic ions can penetrate the satellite shielding surfaces and generate single event effects. High-energy electrons (above 100 keV) can also penetrate the satellite shielding surfaces, resulting in internal charging and electrostatic discharges. Low-energy ions and electrons (below 100 keV) in the geospace environment possess relatively complex behaviors and variations driven by solar wind–magnetosphere interactions associated with the solar and geomagnetic activities, leading to satellite surface charging and subsequent discharging. They are also regarded as one of the major causes of satellite anomalies (Iucci *et al.* 2005, Ishii *et al.* 2021, Ferguson *et al.* 2015; and references therein).

Geosynchronous Earth orbit (GEO) satellites encounter plasma environments with vastly diverse characteristics. The balance of electric potential may be interrupted at the boundaries of those plasma environments (Koons *et al.* 2006). Surface charging or subsequent discharging

* **Corresponding author: Xu Shan**, Hefei National Research Center for Physical Sciences at the Microscale, Department of Modern Physics, University of Science and Technology of China, Hefei, 230026, China, e-mail: xshan@ustc.edu.cn

Bin Miao, Yiren Li, Kai Liu, Zhenpeng Su, Chenglong Shen, Zonghao Pan, Xin Li, Xinjun Hao: Deep Space Exploration Laboratory/School of Earth and Space Sciences, University of Science and Technology of China, Hefei, 230026, China

Zhe Cao, Zhenyu Sun, Shubin Liu, Qi An: State Key Laboratory of Particle Detection and Electronics (IHEP-USTC), Department of Modern Physics, University of Science and Technology of China, Hefei, 230026, China

Sanbiao Qu, Xingyu Guo, Xiangjun Chen: Hefei National Research Center for Physical Sciences at the Microscale, Department of Modern Physics, University of Science and Technology of China, Hefei, 230026, China

Xiaoping Yang: Shandong Institute of Space Electronic Technology, Yantai, 264003, China

Chao Tian, Yu Jiang: State Key Laboratory of Astronautic Dynamics, Xi'an Satellite Control Center, Xi'an 710043, China

Yuming Wang: Deep Space Exploration Laboratory/School of Earth and Space Sciences, University of Science and Technology of China, Hefei, 230026, China; CAS Center for Excellence in Comparative Planetology/CAS Key Laboratory of Geospace Environment, University of Science and Technology of China, Hefei, 230026, China

is a serious challenge for satellites (Thomsen *et al.* 2013, Ganushkina *et al.* 2021, Spence *et al.* 1993, Nicolaou *et al.* 2020, Matéo-Vélez *et al.* 2018). GEO satellites usually encounter surface charging around the Spring and Autumn equinox points. The photoelectrons suddenly decrease in the Earth's shadow and the satellites may be charged to a negative potential of several hundred volts, even several kilovolts. The hot plasma flux during geomagnetically active periods may also break the electric potential balance and charge the satellites. The *in situ* low-energy ion measurements may offer an alternative way to study surface charging (Sarno-Smith *et al.* 2016). On the one hand, the low-energy ion measurements could directly reflect the ion acceleration by the negative satellite potential. On the other hand, the low-energy ion measurements could partially signify the geomagnetic activity level. The top-hat hemispherical or toroidal electrostatic analyzer (ESA) (Carlson *et al.* 1982, Young *et al.* 1988) has been widely used to detect the space low-energy ions in most missions such as Wind (Lin *et al.* 1995), Cluster (Rème *et al.* 1997), FAST (Carlson *et al.* 2001), Venus Express (Barabash *et al.* 2007), Van Allen probes (Spence *et al.* 2013), GOES (Dichter *et al.* 2015), MAVEN (Halekas *et al.* 2015), and Tianwen-1 (Kong *et al.* 2020).

In this article, a miniaturized low-energy ion spectrometer (LEIS) payload onboard a Chinese GEO satellite is presented. This payload inherited our previous instrument for the SJ18 mission (Hu *et al.* 2019), employing a state-of-the-art cooperative design of a top-hat ESA and a

pair of angular scanning deflectors to obtain a $360^\circ \times 90^\circ$ large field of view (FOV). Further improvement of its capability is achieved in detecting the space ions with a wider energy range from 50 eV to 25 keV/q and higher resolutions. The LEIS is able to sample the energy flux distributions of ions in 3D space, measure the negative spacecraft surface charging, and monitor the space environment variations associated with magnetospheric storms or substorms.

2 Design of the LEIS payload

The recently launched Chinese navigation satellite is a three-axis stabilized spacecraft in GEO orbit, located at a geocentric distance of 6.6 Re in the geographical equatorial plane as illustrated in Figure 1(a). The typical top-hat ESA (Carlson *et al.* 1982, Young *et al.* 1988) has a 360° azimuthal FOV, but only a few degrees for the elevation angles. To obtain a larger FOV of the ESA on a three-axis stabilized spacecraft, a state-of-the-art design is developed by supplementing a pair of angular scanning deflectors into a typical top-hat ESA. The present LEIS payload is an update of our heritage instrument (Hu *et al.* 2019), persisting a large FOV coverage of 360° azimuthal angles and 90° elevation angles. Relative to the previous spectrometer, the present design increased the inner sphere radius and reduced the separation between the inner

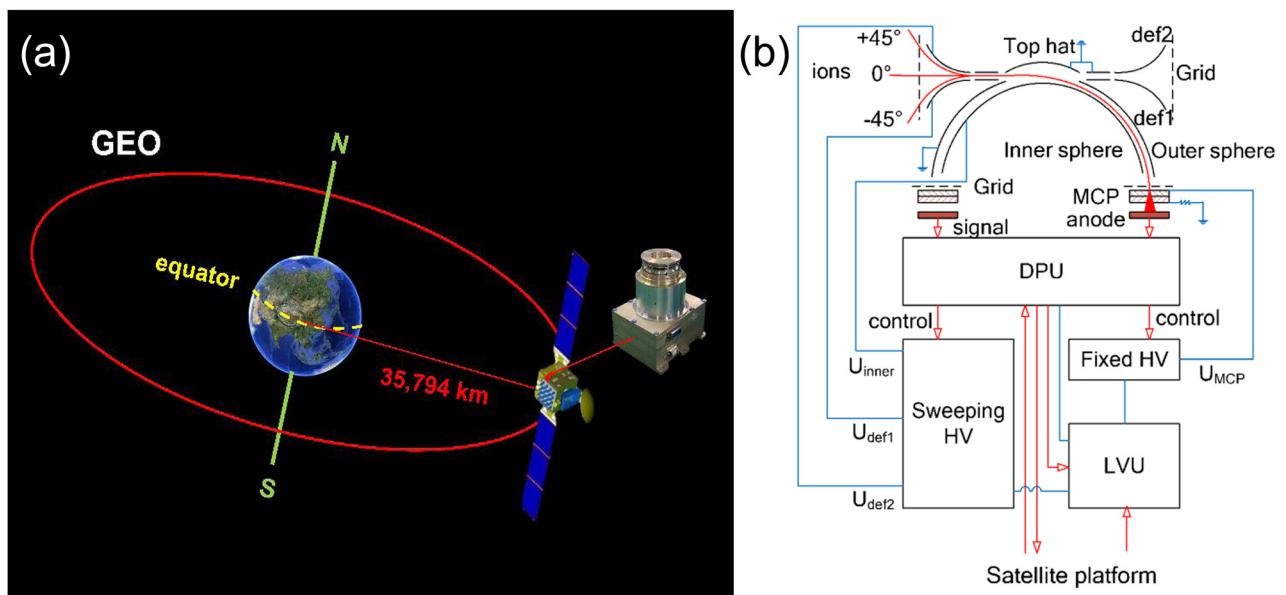


Figure 1: (a) Schematic diagram of the satellite flying along the GEO orbit around the Earth. The inset photograph is a flight model of the LEIS payload. (b) Structural and functional schematic diagram of the LEIS payload.

and outer spheres. Such key changes can enable us to achieve much higher energy and angular resolutions, as well as a larger analyzer constant that can make the detected energy range extend up to 25 keV/q even if keeping the same range of sphere bias voltage. In addition, the electronic and power supply systems have been further optimized and compacted to fulfill smaller power consumption, weight, and sizes. The present LEIS specifications are listed in Table 1.

The LEIS payload mainly consists of two parts: a sensor head and an electronic box. In Figure 1(a), the insert photograph is its flight model. Figure 1(b) shows its structural and functional schematics. The sensor head is a rotationally symmetric structure including a pair of angular scanning deflectors (signed as def1 and def2), a top-hat ESA, and a position-sensitive detector. The top-hat ESA has an inner sphere electrode (radius $R_1 = 36$ mm), an outer sphere electrode (radius $R_2 = 38$ mm), and a small “top-hat” section (radius $R_3 = 40$ mm). The position sensitive detector (PSD) is composed of a pair of annular microchannel plates (MCPs) and 16 discrete anodes. As the ESA works, the outer sphere, top hat, and collimator electrodes are grounded, while two deflectors and the inner sphere electrodes are applied to the required voltages. The elevation angles of incident ions from -45° to $+45^\circ$ are selected by scanning the deflector voltages (U_{def1} and U_{def2}). The ion energies are analyzed by sweeping ESA bias voltages (*i.e.*, U_{inner}). After the selection of deflector and ESA voltages, the incident angles and energies of ions are known. These ions can pass through the ESA and hit the PSD positioned at the ESA exit. The produced charge pulses are collected by

the 16 discrete anodes, each anode corresponding to 22.5° azimuth angles (signed as 16 channels from Ch00 to Ch15).

The electronic box includes a digital processing unit (DPU), a high-voltage power supply unit (HVU), and a low-voltage power supply unit. Figure 2 presents the DPU schematics and photographs of the printed circuit board (PCB). Sixteen-channel analog signals that are output from 16 discrete anodes in the sensor head are fast amplified and transferred into digital signals by 16 independent low-noise charge-sensitive amplifier/discriminators (A121). The threshold of each A121 chip for the input signal can be adjusted remotely by changing the reference voltage on the basis of our specially designed self-test module. The radiation-hardened DPU is developed on the basis of an antifuse Field Programmable Gate Array for data acquisition, processing, and storage, as well as the control of HV (high voltage) power supplies, self-test, status monitor, and communication. Two types of memory devices of electrically erasable programmable read only memory (EFROM) and static random access memory (SRAM) are applied to store the parameters of different HV values and the measured data of the payload, respectively. The RS422 communication method is employed to receive instructions from the satellite and respond to the satellite. A user-defined serial protocol is used to upload scientific data to the satellite.

Figure 3 shows the HVU schematics and its PCB photograph, which involve three sweeping HV power supplies and a fixed HV supply. To achieve the sweeping and fixed HV outputs, a widely used cooperation of optocouplers with negative and positive HV modules is employed. Two bipolar sweeping HV supplies (-3 kV to $+3$ kV) are designed specifically and applied on a pair of entrance deflectors. One unipolar sweeping negative HV (0 to -3 kV) is placed on the inner sphere electrode, and an adjustable negative HV (0 to -3 kV) is ready for the MCP electrodes. The low voltages required by the DPU and HV power supplies are conveniently obtained through the conversion of a primary power supply from the satellite platform in a low voltage board.

Operation modes of the present payload have inherited our previous design (Hu *et al.* 2009). Only a brief description is presented here. In the self-test mode, fundamental functions and parameters of the instrument can easily be tested on the basis of the specially designed self-test circuit module. In the normal measurement, the voltages of U_{inner} (0 to -3 kV), U_{def1} , and U_{def2} (-3 kV to $+3$ kV) are swept synchronously with an exponential change. Sixty-four basic energy bins with 8.5% of increment step by step are made for covering the ion energies from 50 eV

Table 1: Specifications of the LEIS payload

Main parameters	Capability
Energy range	50 eV to 25 keV/q
Energy resolution ($\Delta E/E$)	8.5%
Analyzer constant K	8.9
FOV (azimuth \times elevation)	$360^\circ \times 90^\circ$ (-45° to $+45^\circ$)
Angular resolution (azimuth \times elevation)	$\sim 5.5^\circ \times 3^\circ$
Time resolution	20 s (2D)/10 min (3D)*
Geometric factor (each channel)	$\sim 1.6 \times 10^{-4}$ cm ² sr eV/eV
Data rate	11.52 kbps (instantaneous)/ 360 bps (average)
Power	4.8 W
Weight	4.5 kg
Envelope size	210 mm \times 190 mm \times 236 mm

*Time resolution can be improved by adjusting the retention time at each scanning step of energy and angle *via* RS422 instructions.

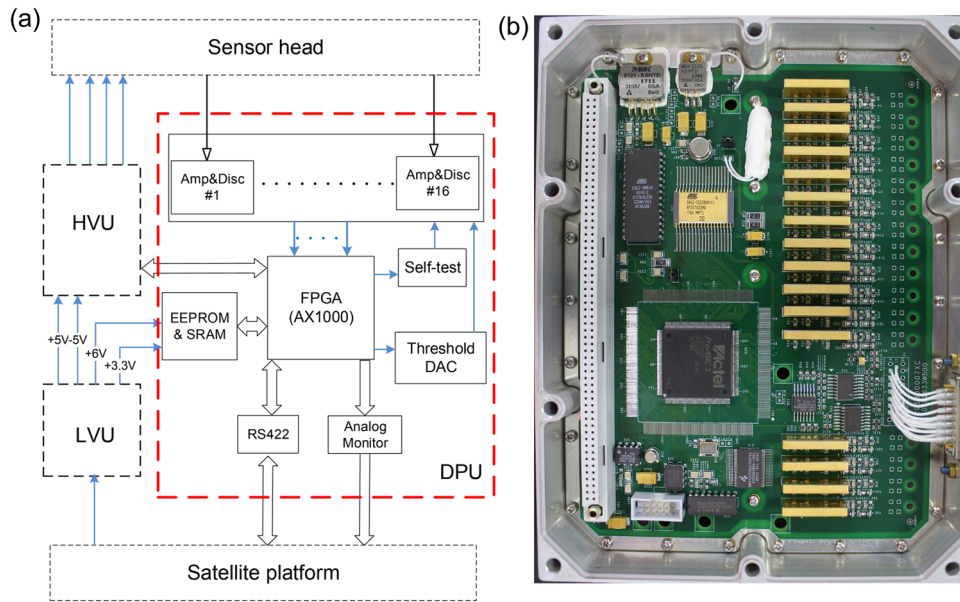


Figure 2: (a) Schematics of the DPU and (b) photograph of its PCB.

to 25 keV/q, and 15 angular bins for the elevation angles from -45° to 45° . Each elevation angle takes 128 steps as a minor cycle including 64 upward and 64 downward sweeping steps. There are 16 minor cycles in which the last cycle is designed for recording the possible UV light response and background noise by setting all sweeping voltages to zero. It is noted that the sweeping steps of HV supplies and the stay time at each of steps can be rearranged via RS422 instructions.

3 Performance of the LEIS payload

3.1 Results of simulation and calibration on the ground

In the design of the payload, we take advantage of Simion software (<http://simion.com>) to study the ESA performance in detail. The methods used in the simulation

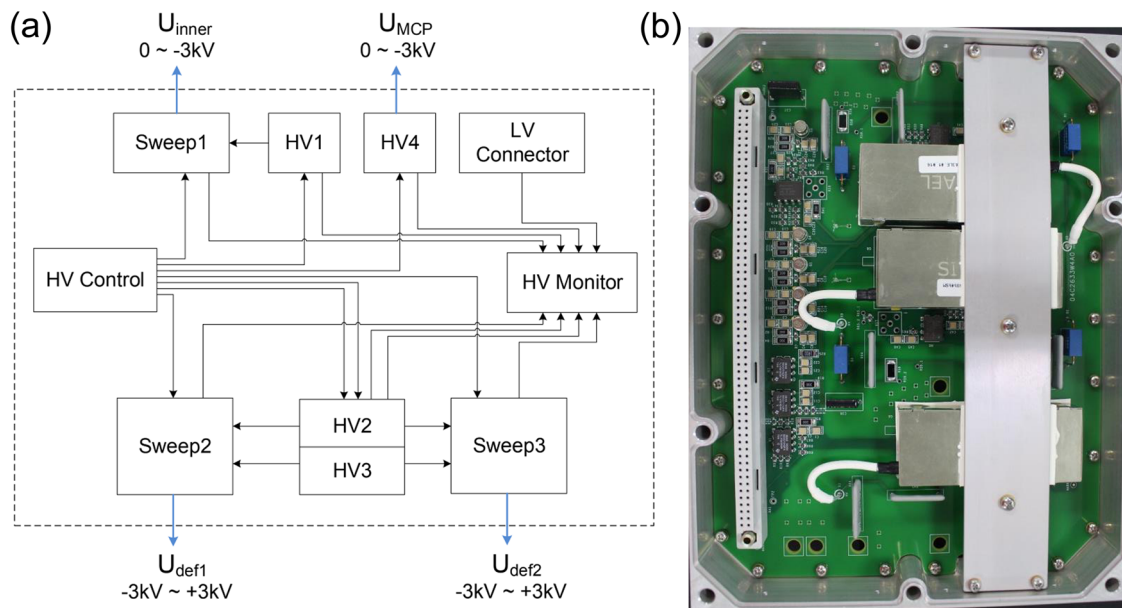


Figure 3: (a) Schematics of the HVU and (b) photograph of its PCB.

have been described previously (Hu *et al.* 2009). A rectangular ion (proton) beam with uniform position distribution is launched and fully covers the ESA entrance. For all small position units of the ion beam, a set number of protons in a bunch with a Gaussian distribution of 30% energy spread are conically emitted along the same established angular direction with small angular spread in a 0.25° increment one by one.

First, we set $U_{\text{def1}} = U_{\text{def2}} = 0$ to study the case that the incident ions with elevation angle $\beta = 0$ fly into the ESA. Under a series of specific sphere bias voltages U_{inner} and variable ion energies from 40 eV to 30 keV, we record the protons that can arrive at the exit of the ESA through the selection of a spherical electric field and find the relation between the ion energy and sphere bias voltage. Figure 4(a) shows the ion energy response of the ESA at a series of U_{inner} , and the peak shapes are almost the same for different

U_{inner} . From the energy response spectra in Figure 4(a), we can obtain the energy resolution $\Delta E/E$ of the ESA as 8.2%, as shown in Figure 4(b). Similarly, we also deduce that the analyzer constant K is 8.9 by fitting the ratio of the energy E/q of ions to ESA bias voltage U_{inner} as shown in Figure 4(c). Note that it is key to obtain the analyzer constant K because this parameter enables us to determine the energy of ions on the basis of sphere bias voltage. We also simulated the responses of ESA to the elevation and azimuth angles of ions, as well as the effective length of ion entrance positions. Figure 4(d) shows the angular distribution of ions at elevation angle $\beta = 0$, and the resolution of the elevation angle is determined to be 2.1° . Figure 4(e) presents the angular distribution of ions at azimuth angle $\alpha = 0$, and the resolution of the azimuth angle is 5.4° . Compared with our previous spectrometer (Hu *et al.* 2019), the present energy and angular resolutions are much better.

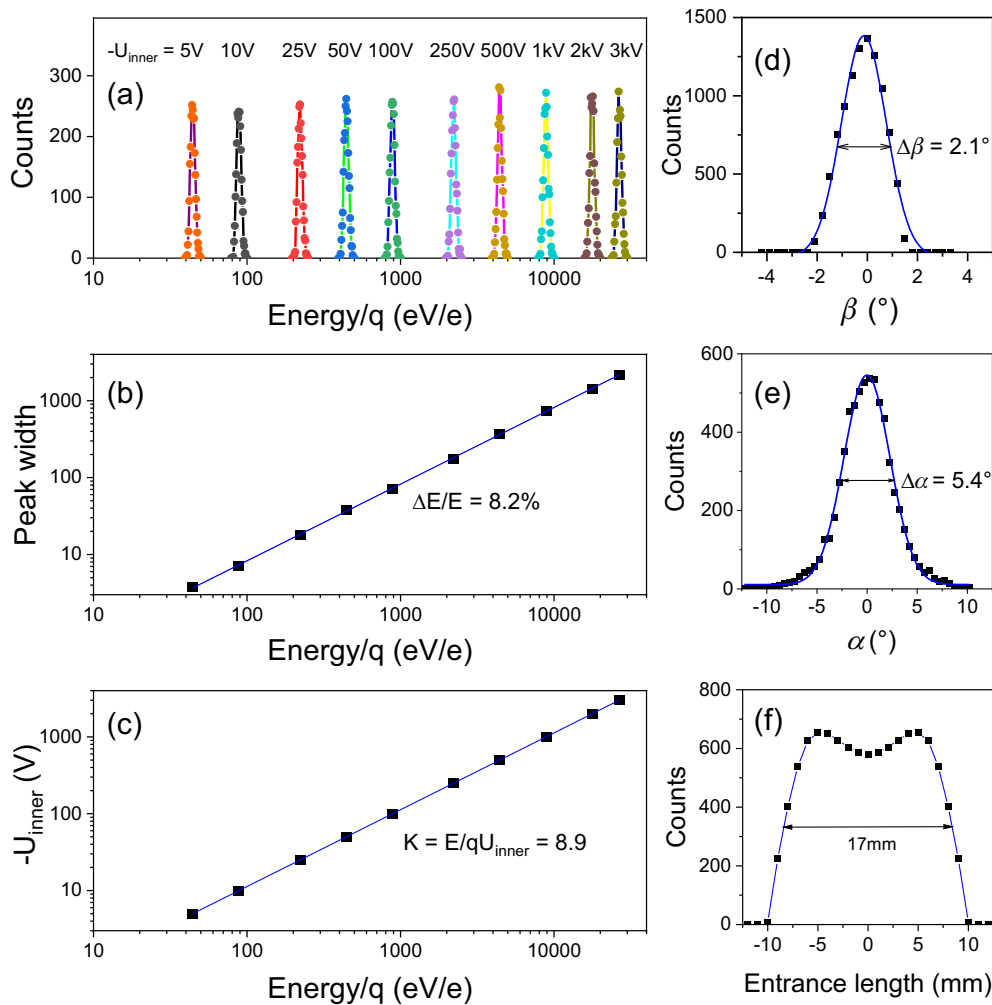


Figure 4: Simulation results: (a) energy response spectrum, (b) energy resolution, (c) analyzer constant K , (d) elevation angle response, (e) azimuth angle response, and (f) effective length of the entrance aperture for the incident ions.

In addition, the present analyzer constant K is larger than the previous one, meaning much wider energy range can be achieved. These obvious improvements of performance are benefitted from the increase of the inner sphere radius and the reduction of the separation between the inner and outer spheres. Figure 4(f) illustrates the entrance position spectrum of the incident ions, and the effective length is estimated to be approximately 17 mm. Taking the entrance aperture $\Delta R = 2$ mm, the active area A_e is approximately 34 mm^2 . Therefore, another key parameter called the geometric factor (GF) can be estimated by the formula $GF = A_e \times \langle \Delta\beta \times \Delta E/E \rangle \times \int \cos \alpha d\alpha$ (Young *et al.* 1988). The present GF of ESA for each 22.5° azimuth angular channel is obtained to be $3.9 \times 10^{-4} \text{ cm}^2 \text{ sr eV/eV}$. Considering the 50% MCP efficiency and the 81% transmittance of two molybdenum grids, the absolute GF for each anode channel is $1.6 \times 10^{-4} \text{ cm}^2 \text{ sr eV/eV}$. Note that the GF directly links the measured count rate to the incident ion energy flux.

To investigate the response of ESA for different elevation angles β of incident ions, we apply voltages to entrance deflectors, satisfying $U_{\text{def1}} = -U_{\text{def2}}$, *i.e.*, the deflecting

voltage $U_{\text{def}} = 2U_{\text{def1}} = -2U_{\text{def2}}$. A series of angles are chosen from -45° to 45° as the elevation angles of incident ions, and the voltages of U_{inner} , U_{def1} , and U_{def2} are swept synchronously. The elevation angle β of incoming ions is determined by the voltage U_{def} and the energy E/q of the ions. Figure 5(a) depicts the elevation angular spectrum with the change of $U_{\text{def}}/(E/q)$, in which the normalized GFs for different β are extracted and plotted in Figure 5(c). Relative to that at $\beta = 0^\circ$ ($3.9 \times 10^{-4} \text{ cm}^2 \text{ sr eV/eV}$), there is a small difference for different β values. The resolution of the elevation angles is therefore estimated to be less than 3° , as shown in Figure 5(d). From Figure 5(a), we can obtain the relation between the elevation angle and $U_{\text{def}}/(E/q)$, which can be fitted well by a linear function $\beta = 126.31U_{\text{def}}/(E/q) + 0.133$, as shown in Figure 5(b). This function plays an important role in determining the elevation angle of specific energy ions according to the sweeping voltage; that is, under the given voltages of entrance deflectors and the inner sphere, the energy and elevation angle of incident ions can be determined.

The calibration experiment was carried out by employing our developed vacuum test facility, which was described previously (Hu *et al.* 2019). Due to the limitation of unavailable

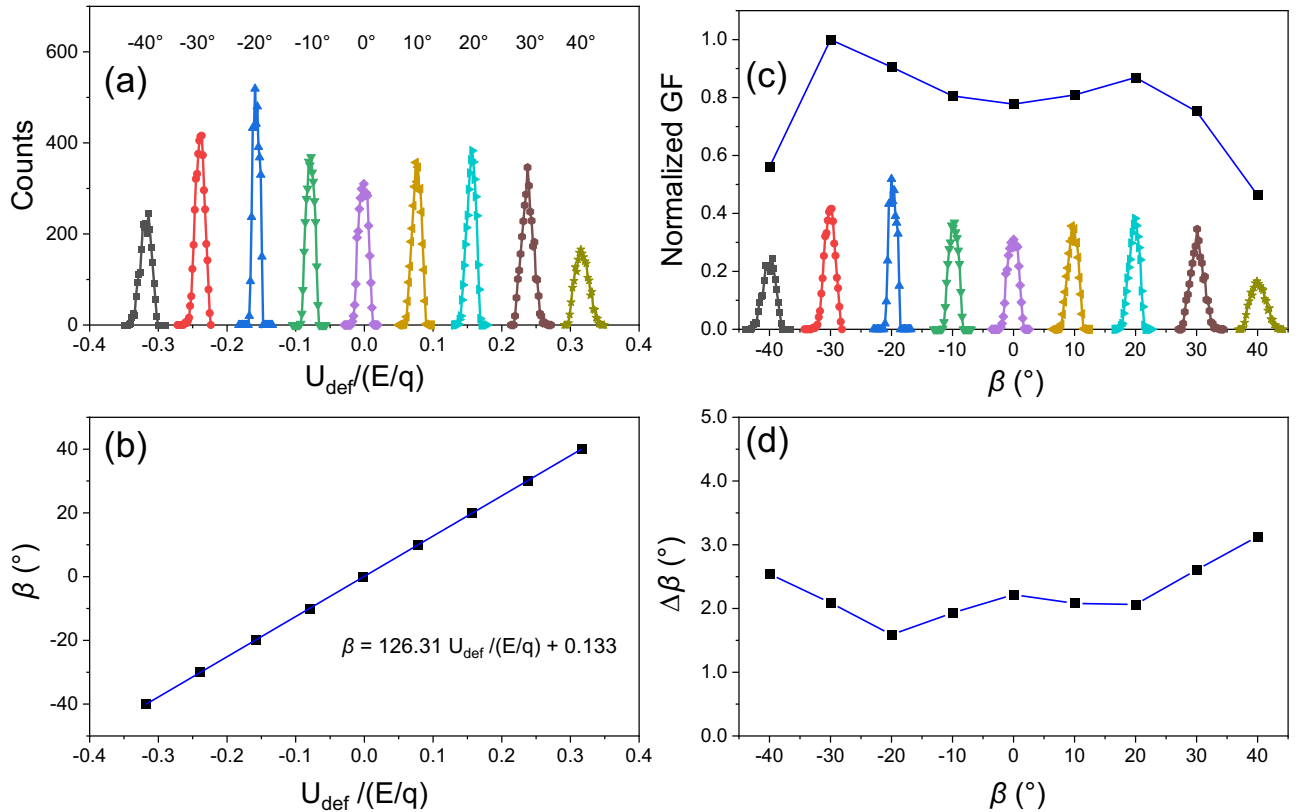


Figure 5: Simulation results for different elevation angles: (a) Elevation angular spectrum as the function of $U_{\text{def}}/(E/q)$, (b) the linear relationship between the elevation angle β and $U_{\text{def}}/(E/q)$, (c) the normalized GF for different elevation angles, and (d) the elevation angular resolution.

beam time of ion accelerator facility used previously, a sketchy Penning ionization ion gun was used. In the experiment, several specific energies were chosen to obtain the energy response spectra and the analyzer constant. The elevation angles and azimuth angles were varied by rotating the LEIS payload through the 3-axis turntable. The ion beam flux is measured using a faraday cup that is moved in and out of the beam at the location of the sensor aperture. For a series of specific ion angle and energy, the voltages of U_{inner} , U_{def1} , and U_{def2} are swept synchronously and the counts of ions that hit the PSD are recorded. Consequently, there are many energy and angle response spectra obtained at different energies, 14 elevation angles, and 16 azimuth angles. Here, only a part of them is presented. Figure 6 shows the experimental results for 1 of 16 azimuth angle channels (Ch06) at different ion energies and elevation angles. The energy response spectrum is presented in Figure 6(b), from which the peak positions are obtained for the corresponding energies. The analyzer constant is therefore deduced and plotted in Figure 6(c). Through a linear function fit, the analyzer constant is determined to be $K = 8.94$ (i.e., the slope of the line), which is very close to the simulated value of 8.9. Because the range of ion energy is limited from 1,000 to 4,000 eV and the energy is not monochromatic, present calibration experiments were not enough to cover the whole energy range and to truly evaluate the

energy resolution. Detailed simulations made up for the shortage of calibration experiments. Figure 6(c) depicts the elevation angular spectrum measured at a specific energy ($E/q = 3,000$ eV/e), from which the angular resolution can be estimated to be about 3° and it is consistent with the simulation. From the measured incident ion current and the counts from energy and angular response spectrum, the GF is estimated to be $\sim 1.0 \times 10^{-4}$ cm^2 sr eV/eV. Furthermore, according to the elevation angles and the corresponding deflector voltages, the relationship between the elevation angle β and $U_{\text{def}}/(E/q)$ is obtained and plotted in Figure 6(d). Fitting the data by a linear function, we obtained $\beta = 115.78 U_{\text{def}}/(E/q) + 2.07$ that generally reproduces the simulation result. The small difference between experiment and simulation probably come from the uncertainty in experiments such as ion energy and angle values.

3.2 Preliminary results of on-orbit measurement

The LEIS payload fulfilled the degassing at a suitable period of time after the satellite launch. Subsequently, within the permitted time, inflight tests were performed

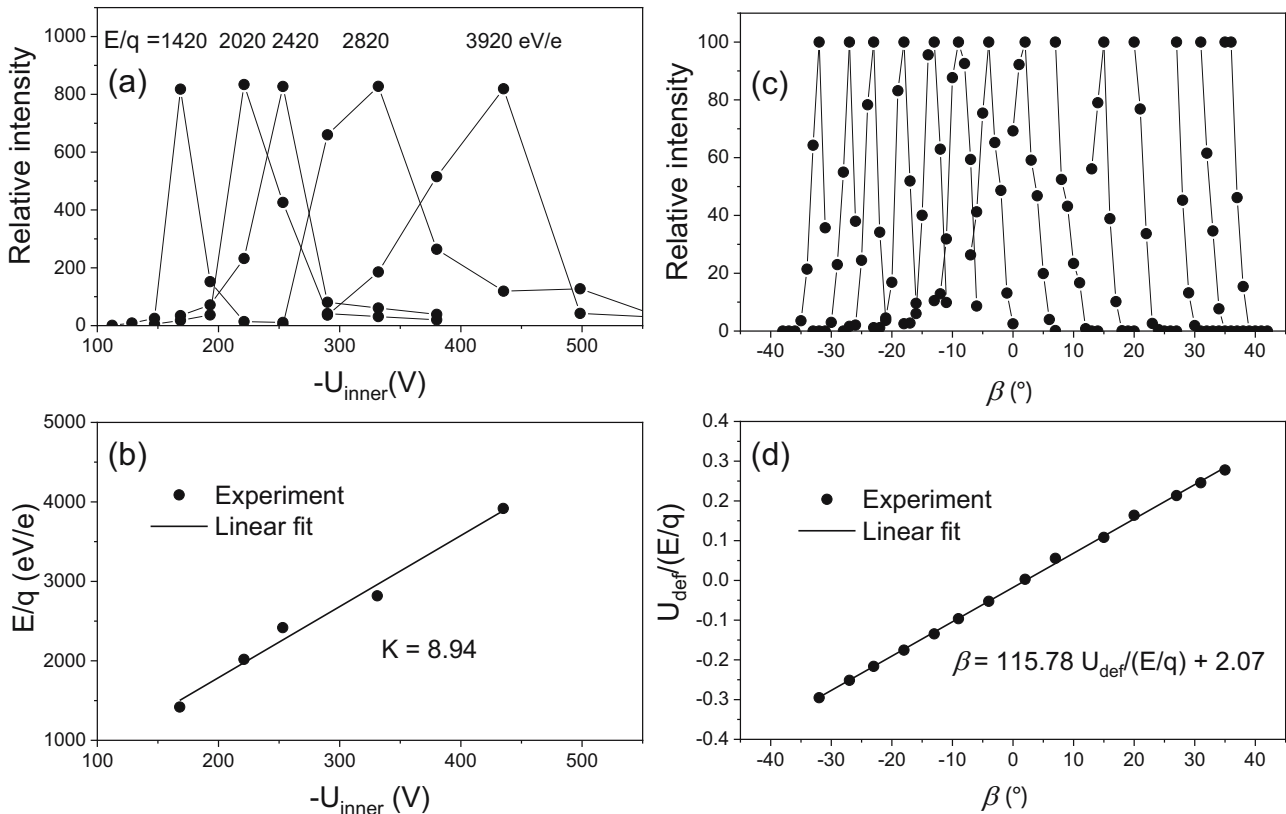


Figure 6: Calibration experimental results: (a) energy response spectrum, (b) analyzer constant K , (c) elevation angle response spectrum, and (d) the linear relationship between the elevation angle β and $U_{\text{def}}/(E/q)$.

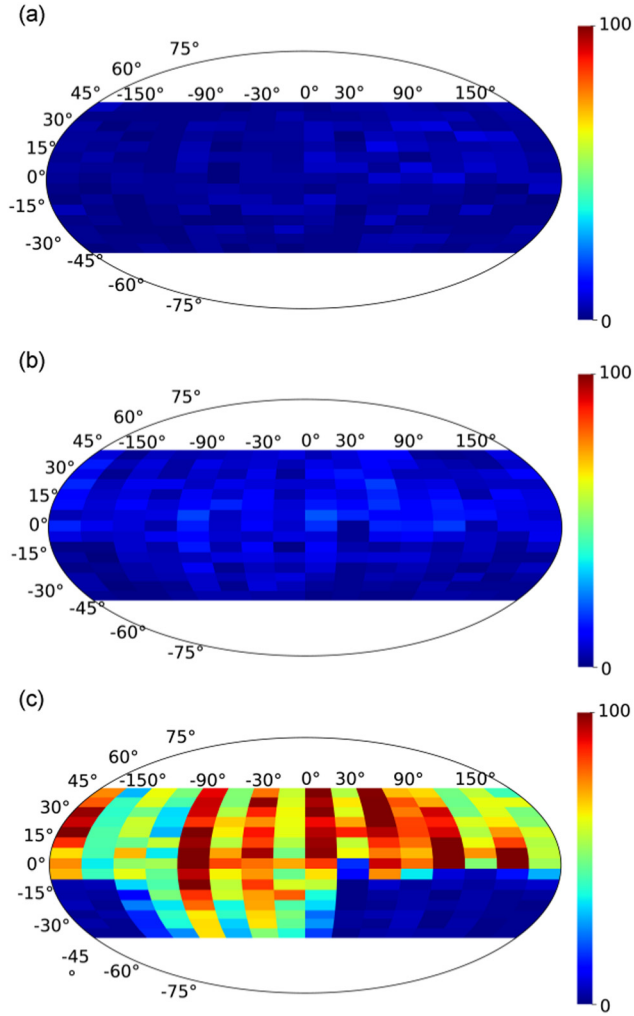


Figure 7: Raw data from on-orbit measurement in the instant time of 0.2 s for (a) 584 eV energy bin with 8.5% bandwidth, (b) 4,000 eV energy bin with 8.5% bandwidth, and (c) 22,666 eV energy bin with 8.5% bandwidth.

including electronics self-checking, HV operation, data storage and transmission, communication with ground stations, *etc.* Furthermore, the adjustment and optimization of amplifier thresholds and MCP voltages have been made *via* RS422 instructions. The normal ion measurement started on September 24, 2021. In light of the work scheme introduced above in which the voltages of U_{inner} , U_{def1} , and U_{def2} are applied by sweeping synchronously with an exponential variation, three-dimensional (3D) measurements on energetic ions in space with a large FOV of $360^\circ \times 90^\circ$ and a wide energy range up to 25 keV/q have been achieved. As an example, Figure 7 presents the raw data from on-orbit measurement in the time of 0.2 s for the individual 584, 4,000, and 22,666 eV energy bins with 8.5% bandwidths. Since the density of

space ions in GEO is extremely small, the statistic counts recorded in a very short time for one energy bin are not large but visible. Note that the higher counts observed in 22,666 eV energy bin are because this bin has a larger energy bandwidth. In addition, it is much easier to see from Figure 7(c) that the ions from certain elevation angles cannot be detected by several channels due to the shielding of the spacecraft itself.

Based on the raw data measured over a relatively long time, the energy and flux distributions of ions in GEO space can be obtained according to the instrumental parameters and the applied voltages. The energy of ions is determined by the product of the analyzer constant ($K = 8.9$) and the ESA bias voltage. The differential energy flux of ions is obtained by the quotient of the recorded counts and the GF ($\text{GF} = 1.6 \times 10^{-4} \text{ cm}^2 \text{ sr eV/eV}$). In the data processing, to obtain the true ion data, we deducted the background noise and possible UV contamination, which can be derived by the counts recorded at the last time of each cycle period in which the voltages of U_{inner} , U_{def1} , and U_{def2} are all set to zero.

Figure 8 presents the preliminary results recorded on-orbit by different azimuth angle channels (Ch00, Ch04, Ch08, and Ch12) in a day from 2021-09-30 to 2021-10-01. This universal time (UT) corresponds to one magnetic local time (MLT) 12:00 and the next adjacent MLT 12:00. One can see from Figure 8(a1–a4) that the measured initial data are contaminated by the background noises and solar UV light response. Figure 8(b1–b4) shows the data from the background noises and solar UV light response obtained *via* the specially designed way. At the first glance, the bright pillars are easily found, which represent the UV response. The satellite position varies continually in a day; that is, each azimuth angle channel faces the Sun at different times. The on-orbit measurement results revealed in this case that the strong UV response for different channels emerged at different times. Figure 8(c1–c4) presents the true ion data obtained by using the initial data to subtract the background noises and UV response. For all channels, the recorded data display the identical remarkable enhancements of ion fluxes at the specific energy region (*e.g.*, below 1 keV or above 10 keV) and a certain time of a day (*e.g.*, MLT 00:00), which suggests the occurrence of surface charging or substorm events.

Figure 9 presents the ion energy and flux results measured by a representative channel (Ch05) at UT time from 2021-09-24/04:29 to 2021-10-03/04:29. As the figure shows, noticeable flux enhancements of ions with energies above 2 keV are observed clearly, like flying ribbons, indicating

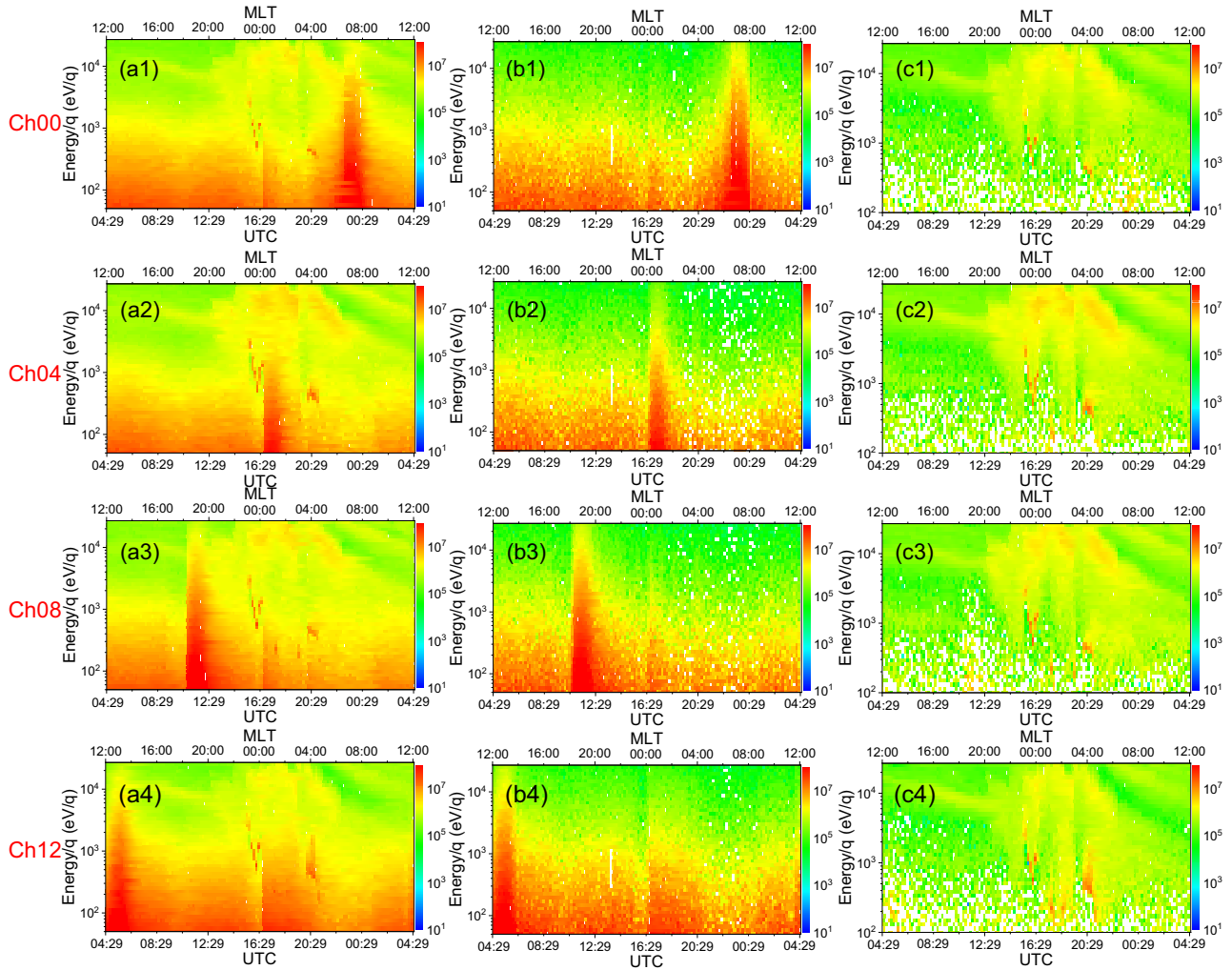


Figure 8: Preliminary results recorded on-orbit by different azimuth angle channels in a day from 2021-09-30 to 2021-10-01. The panels in the left column are the initial data. The panels in the middle column are the UV response and background noise. The panels in the right column are the true ion data obtained by using the initial data to subtract UV response and background noise. (a1, b1 and c1) for Ch00, (a2, b2 and c2) for Ch04, (a3, b3 and c3) for Ch08, and (a4, b4 and c4) for Ch12.

the signature of substorm occurrences. The local bright lines in the low-energy region of hundreds of eV are the results of spacecraft surface charging. Figure 9(b) shows the variation of ion fluxes recorded in 1 day from 2021-09-30/04:29 to 2021-10-01/04:29. One can easily see that the significant flux changes occurred at midnight and dawn-side, revealing the intensive plasma injection signatures associated with the possible storm/substorm or surface charging events. When the spacecraft surface has a negative potential, the incoming ions can accelerate and then enter the ESA. As a result, the recorded energy achieves the increasing change relative to the initial energy. In other words the initial ions with energies smaller than the amount of surface potential will be directly speeded up and

recorded in the same energy bins, resulting in significantly enhanced counts in such energy bins. As shown in Figure 9(b), an ion accumulation appeared in ~ 1 keV energy bins near MLT 00:00 and the other one occurred in ~ 500 eV energy bins near MLT 04:00, suggesting two possible surface charging signatures. The charging sustained for approximately 2 h. Therefore, the charging potential on the spacecraft surface can be deduced on the basis of the sudden enhancement of ion fluxes. In the present two cases, the electric potential on the satellite surface is determined to be about -500 V, even up to -2 kV. The further observation on magnetic storm/substorm or surface charging and their evolutions over much longer times will be presented in an article to be appeared (Shan *et al.* 2022).

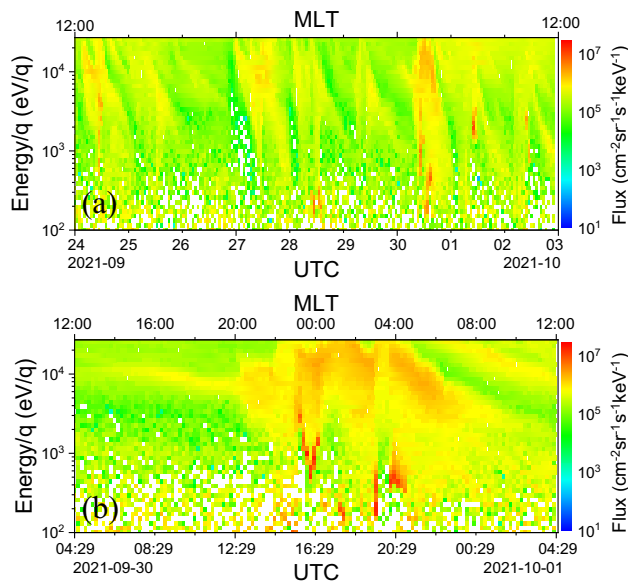


Figure 9: Differential energy flux of ions measured by Ch05 during (a) 2021-09-24 to 2021-10-03 and (b) 2021-09-30 to 2021-10-01.

4 Summary

In this article, we report an LEIS developed for a Chinese navigation satellite in geosynchronous orbit. An advanced design combining a top-hat ESA with a pair of angular scanning deflectors enables us to achieve *in situ* measurement of low-energy ions in 3D space with a large FOV of $360^\circ \times 90^\circ$ and a wide energy range from 50 eV to 25 keV per charge. The performance of the LEIS payload has been evaluated in detail by a series of simulations, calibration experiments, and environmental tests on the ground, as well as the measurements in flight along the satellite orbit. The preliminary results from on-orbit observations demonstrate that the capability of the present LEIS payload can well meet the mission requirements for sampling the low-energy ion distributions in 3D space, measuring the negative satellite potential, and monitoring the magnetospheric storm or substorm activities.

Acknowledgements: The authors would like to thank all the collaborators from the Shandong Institute of Space Electronic Technology and China Academy of Space Technology for their help in the fabrication and environmental tests of this payload.

Funding information: The work was supported by grants from the Chinese Academy of Sciences (Nos XDB41000000, QYZDB-SSW-DQC015) and the National Natural Science Foundation of China (No. 42188101).

Author contributions: X.S. carried out the spectrometer design and data analysis and wrote the manuscript. B.M. and X.G. dealt with the data and took part in the discussion. Z.C., Z.S, S.L., and Q.A. carried out the electronics design. B.M. and Y.L. carried out the calibration experiment. S.Q. and X.S. carried out the simulations. Z.C., Z.S., Y.L., K.L, Z.P., X.L., X.H., and X.Y. took part in the manufacture. C.T. and Y.J. took part in the on-orbit control and data transmission. Z.S, C.S., X.C., and Y.W. took part in the discussion and gave valuable suggestions. X.S. and Y.W. supervised the work. All the authors discussed the results and commented on the paper.

Conflict of interest: The authors declare no competing interest.

References

- Baker DN. 2000. The occurrence of operational anomalies in spacecraft and their relationship to space weather. *IEEE Trans Plasma Sci.* 28:2007–2016.
- Barabash S, Sauvaud JA, Gunell H, Andersson H, Grigoriev A, Brinkfeldt K, et al. 2007. The analyser of space plasmas and energetic atoms (ASPERA-4) for the venus express mission. *Planet Space Sci.* 55:1772–1792.
- Carlson CW, Curtis DW, Paschmann G, Michel W. 1982. An instrument for rapidly measuring plasma distribution functions with high resolution. *Adv Space Res.* 2:67–70.
- Carlson CW, McFadden JP, Turin P, Curtis DW, Magoncelli A. 2001. The electron and ion plasma experiment for fast. *Space Sci Rev.* 98:33–66.
- Dichter BK, Galica GE, McGarity JO, Tsui S, Golightly MJ, Lopate C. 2015. Specification, design, and calibration of the space weather suite of instruments on the NOAA GOES-R program spacecraft. *IEEE Trans Nucl Sci.* 62:2776–2783.
- Ferguson DC, Worden SP, Hastings DE. 2015. The space weather threat to situational awareness, communications, and positioning systems. *IEEE Trans Plasma Sci.* 43:3086–3098.
- Ganushkina NY, Swiger B, Dubyagin S, Mateo-Velez JC, Liemohn MW, Sicard A, et al. 2021. Worst-case severe environments for surface charging observed at LANL satellites as dependent on solar wind and geomagnetic conditions. *Space Weather.* 19:e2021SW002732.
- Halekas JS, Taylor ER, Dalton G, Johnson G, Curtis DW, McFadden JP, et al. 2015. The solar wind ion analyzer for MAVEN. *Space Sci Rev.* 195:125–151.
- Hu RX, Shan X, Yuan GY, Wang SW, Zhang WH, Qi W, et al. 2019. A low-energy ion spectrometer with half-space entrance for three-axis stabilized spacecraft. *Sci China Tech Sci.* 62:1015–1027.
- Ishii M, Shiota D, Tao C, Ebihara Y, Fujiwara H, Ishii T, et al. 2021. Space weather benchmarks on Japanese society. *Earth Planet Space.* 73:108.
- Iucci N, Levitin AE, Belov AV, Eroshenko EA, Ptitsyna NG, Villoresi G, et al. 2005. Space weather conditions and spacecraft anomalies in different orbits. *Space Weather.* 3:S01001.

- Kong LG, Zhang AB, Tian Z, Zheng XZ, Wang WJ, Liu B, et al. 2020. Mars Ion and Neutral Particle Analyzer (MINPA) for Chinese Mars Exploration Mission (Tianwen-1): Design and ground calibration. *Earth Planet Phys.* 4:333–344.
- Koons, H., Mazur J, Lopatin A, Pitchford D, Bogorad A, Herschitz R. 2006. Spatial and temporal correlation of spacecraft surface charging in geosynchronous orbit. *J Spacecr Rocket.* 43:178–185.
- Lin RP, Anderson KA, Ashford S, Carlson C, Curtis D, Ergun R, et al. 1995. A three-dimensional plasma and energetic particle investigation for the wind spacecraft. *Space Sci Rev.* 71:125–153.
- Matéo-Vélez JC, Sicard A, Payan D, Ganushkina N, Meredith NP, Sillanpää I. 2018. Spacecraft surface charging induced by severe environments at geosynchronous orbit. *Space Weather.* 16:89–106.
- Nicolaou G, Wicks RT, Rae IJ, Kataria DO. 2020. Evaluating the performance of a plasma analyzer for a space weather monitor mission concept. *Space Weather.* 18:e2020SW002559.
- Quan L, Liu Y, Li L, Wang D, Wang K, Xue L, et al. 2022. Study on matching between environmental warning information and spacecraft anomalies. *J Spacecr Rocket.* 59:1455–1462. <https://arc.aiaa.org/doi/10.2514/1.A35173>.
- Rème H, Bosqued JM, Sauvaud JA, Cros A, Dandouras J, Aoustin C, et al. 1997. The cluster ion spectrometry (CIS) experiment. *Space Sci Rev.* 79:303–350.
- Sarno-Smith LK., Larsen BA, Skoug RM, Liemohn MW, Breneman A, Wygant JR, et al. 2016. Spacecraft surface charging within geosynchronous orbit observed by the Van Allen Probes. *Space Weather.* 14:151–164.
- Shan X, Miao B, Cao Z, Sun ZY, Li YR, Liu K, et al. 2022. First results of the low energy ion spectrometer onboard a Chinese geosynchronous satellite. *Sci China Tech Sci.* <https://www.sciengine.com/SCTS/doi/10.1007/s11431-022-2143-6>.
- Spence HE, Blake JB, Fennell JF. 1993. Surface charging analysis of high-inclination, high-altitude spacecraft: Identification and physics of the plasma source region. *IEEE Trans Nucl Sci.* 40:1521–1524.
- Spence HE, Reeves GD, Baker DN, Blake JB, Bolton M, Bourdarie S, et al. 2013. Science goals and overview of the radiation belt storm probes (RBSP) energetic particle, composition, and thermal plasma (ECT) suite on NASA's Van Allen probes mission. *Space Sci Rev.* 179:311–336.
- Thomsen MF, Henderson MG, Jordanova VK. 2013. Statistical properties of the surface-charging environment at geosynchronous orbit. *Space Weather.* 11:237–244.
- Young, DT, Bame SJ, Thomsen MF, Martin RH, Burch JL, Marshall JA. 1988. 2π -radian field-of-view toroidal electrostatic analyzer. *Rev Sci Instrum.* 59:743–751.